

JOURNAL OF SUSTAINABLE ENGINEERING AND TECHNOLOGY

JOURNAL OF SUSTRINABLE ENGINEERING AND TECHNOLOGY
TRACKET

PROTECTION

TO STATE OF THE PROTECTION OF T

Journal homepage: www.joset.com.ng

Numerical Study of Performance of Airfoil with Sinusoidal-Shaped Leading Edge at Low Wind Speed

Bashir Isyaku Kunya¹, Yusuf Alhassan², Faisal Balarabe³, Musa Alhaji Ibrahim⁴, Salisu Isyaku Kunya⁵ ^{1.2,3,4} Department of Mechanical Engineering, Aliko Dangote University of Science and Technology, P.M.B. 3244, Wudil, Kano, Nigeria

⁵ Department of Science Laboratory Technology, Jigawa State Polytechnic, Dutse

ARTICLE INFO

Article History

Received: 03 Dec 2024 Accepted: 17 Feb 2025 Published: 18 April 2025

Corresponding Author:

Bashir Isyaku Kunya Mechanical Engineering Department, Faculty of Engineering, Aliko Dangote University of Science and Technology, Wudil, P.M.B 3244, Kano, Nigeria kunyabashir@kustwudil.edu.ng

ABSTRACT

Increasing the airfoil's angle of attack is one way to enhance its performance. The biggest issue, though, is that an airfoil will eventually stall when its angle of attack increases beyond its operating angle. The performance of an airfoil could be improved by a technology that allows increasing its operating angle. This study uses airfoils with NACA 4412 cross-section profiles to numerically simulate how sinusoidal bumps, sometimes known as tubercles, at an airfoil's leading edge affect performance. Two computational software, GAMBIT and Fluent, were employed. The simulation was conducted using the shear stress transport $(k-\omega)$ turbulence model. The parameters examined at low Reynolds number based on 6 m/s air velocity are lift, drag, angle of attack, bump height, and flow separation (or stall). The results show that the convectional airfoil model achieved a higher maximum lift coefficient than the bumpy airfoil between 5-degree and 15-degree angles of attack but quickly dropped below that of the bumpy airfoils due to stall effects. The max lift coefficient for the convectional airfoil is 1 at around 12-degree angle of attack before dropping, and that of bumpy one stayed at a max of 0.91 from 12degree up to 15-degree. The drag coefficient of the conventional airfoil increases with angle of attack up to 15-degree, and continue to increase along a straight line up to the last angle (25-degree). The bumpy airfoil model drag coefficients variation with angle of attack shows similar trend with that of conventional one, only that between 5 and 20-degree angle of attack, the bumpy airfoil has greater drag coefficients. The lowest and highest drag coefficients for both models are approximately 0.03 and 0.44.

Keywords: Angle of attack · lift coefficient · drag coefficient · bumps · NACA 4412

1. Introduction

An airfoil is an elongated stream line body that has a rounded leading edge (LE) and a gradual curvature in the direction of flow. When angled properly, the airfoil deflects the incoming air, creating lift force—a force acting on the airfoil in the opposite direction as the deflection. According to Douglas et al. [1], an airfoil's shape and angle of attack (AoA) are the main factors that affect lift. The drag force is simply a resistance force.

One of the primary methods for enhancing an airfoil's performance at low wind speeds is to increase its AoA. The biggest issue is that an airfoil would eventually stall as its AoA increases beyond operating limit [2]. The development of a technique that increases the airfoil's working angle offers the possibility of improving airfoil performance.

The physical nature of the pectoral flippers (fins) of the humpback whale (*megaptera novaeangliae*) may provide solution for improving performance of an airfoil. The flippers have a series of sinusoidal-shaped bumps called tubercles on their LE. The unique LE of the flipper might play a role in the feeding process of these whales. The humpback whale is a species of the largest group of baleen whale with a distinct body shape, long pectoral flippers (fins) and a knobbly head. Its common surface behavior is breaching, tail-lobbing and pectoral fin slapping [3]. The authors further noted the increased maneuverability of humpback whales relative to other baleen whales, and their evolutionary adaptation of the "bubble wall hunting" process where small radius turns are especially beneficial for enhanced feeding success.

Some computational and experimental studies cited in this work can provide a proof of the positive impact of airfoil LE tubercles (bumps) on performance of airfoil the same way it works for humpback whale. For examples, the results of experimental study by Hansen et al. [4] on the influence of bump height, and sinusoidal wavelength at the LE of NASA 65-021 and NASA 0021 foils show that the tubercle LE was more valuable for the NASA 65-021 foil than for the NASA 0021 foil and that both tubercle foils showed improved maximum lift coefficient and a larger stall angle than the conventional foil. The numerical study by Gawad [5] of the effect of tubercles on the flow characteristics around NASA 0012 airfoil found that tubercles delayed stall at a higher AoA, and the maximum value of lift coefficient and the angle at which stall occurs increases with Reynolds number for both the regular and tubercle airfoils. The values of the drag coefficient of tubercle airfoil are greater than those of regular airfoil. Asli et al [6] carried out computational investigation of the effect of protuberances at the LE of a thick airfoil (S809) at 10⁶ Reynolds number and revealed that, at low AoA before the stall region, lift coefficient decreased slightly rather than the baseline model. However, the modified airfoil has a smooth stall trend while the baseline airfoil lift coefficient sharply reduced due to the separation which occurred on a suction side. Similar results were obtained by Kunya et al., [7] who studied numerically and experimentally the effect of varying sinusoidal bumps (or tubercles) height at the LE of airfoil on its efficiency using NASA LS (1)-0413 cross-section profiles. A computational study of the effect of sinusoidal bumps on the LE of airfoil based on NACA 63-012 cross-section profiles was also conducted at low Reynolds number (41075.22). The results show that bumps on the blade LE have advantage at higher AoA by comparing two turbulence models (Shear stress transport (k-ω) and Spalart-Allmaras) [8].

A research work that studied influence of inter-bumps distances (spacing) at airfoil LE using same cross-section profile used by Kunya et al. [7] show that airfoil performance due to LE bumps depends on Reynolds number and bumps spacing, and work better at larger AoA beyond stall angle. The study was conducted by Kunya et al., [9] at Reynolds number of 2.5 X 10⁴, 4.9 X 10⁴, and 7.2 X 10⁴. As Reynolds number increases performance increases between 0- and 15-degree AoA. Bumps spacing has effect on the airfoil performance at low air velocity (that is, at low Reynolds number) at AoA in the range, 12 to 25 degrees.

The preceding studies discovered that the LE tubercles allow airfoil to work at higher AoA before stall (flow separation) would happen, thereby, improving its performance. However, based on the existing literature, this is the first-time research on numerical study of the effect of sinusoidal bumps height at the LE of airfoil with NACA 4412 cross-section profile at low Reynolds Number around 10⁴ was carried out. The preceding studies were done at comparatively higher Reynolds number around 10⁵ and above, and considered different airfoil profiles. Thus, the need to consider other conditions and airfoil section profiles. This study is therefore on computational study of the effect of sinusoidal bumps at the LE of an airfoil with a NACA 4412 cross-section profiles at low Reynolds number (that is, 41075.22, which corresponds to 6 m/s air velocity and 0.1 m airfoil chord length).

2. Methodology

In this study, a numerical simulation of the effect of sinusoidal bumps (or tubercles) at the LE of an airfoil with NACA 4412 cross-section profiles on its performance using two computational software were performed. The GAMBIT 2.3 software was used for creating the models, the fluid domain, and the mesh. The FLUENT 6.3 software was used for the numerical simulation. Shear stress transport (SST k- ω) turbulence model was used for the simulation.

Two airfoil models were created, one with straight LE (conventional airfoil) while the other has sinusoidal LE (bumpy airfoil), and each has NACA 4412 cross-section profiles. The bumpy airfoil model has inter-bumps (or inter-tubercular) distance of 20% airfoil span and bumps height of 6% chord length as with the natural humpback whale flippers. The NACA 4412 airfoil is one of the NACA four series family and has a maximum thickness of 12% with a camber of 4% located 40% back from the airfoil LE (i.e., 0.4C). NACA 4412 airfoil has stall delay advantage and easier to manufacture. The Table 1 shows the NACA 4412 airfoil section co-ordinates [10] used in creating the models.

| Table 1 Co-ordinates | of the NACA 4412 | airfoil section in | percent of airfoil chord |
|-----------------------|------------------|--------------------|--------------------------|
| Table 1. Co oraniates | | | percent of an ion chora |

| Upper surface | | Lower surface | | |
|--|----------|---------------|----------|--|
| Station | Ordinate | Station | Ordinate | |
| 0 | 0 | 0 | 0 | |
| 1.25 | 2.44 | 1.25 | -1.43 | |
| 2.5 | 3.39 | 2.5 | -1.95 | |
| 5 | 4.73 | 5 | -2.49 | |
| 7.5 | 5.76 | 7.5 | -2.74 | |
| 10 | 6.59 | 10 | -2.86 | |
| 15 | 7.89 | 15 | -2.88 | |
| 20 | 8.80 | 20 | -2.74 | |
| 25 | 9.41 | 25 | -2.50 | |
| 30 | 9.76 | 30 | -2.26 | |
| 40 | 9.80 | 40 | -1.80 | |
| 50 | 9.19 | 50 | -1.40 | |
| 60 | 8.14 | 60 | -1.00 | |
| 70 | 6.69 | 70 | -0.65 | |
| 80 | 4.89 | 80 | -0.39 | |
| 90 | 2.71 | 90 | -0.22 | |
| 95 | 1.47 | 95 | -0.16 | |
| 100 | 0.13 | 100 | -0.13 | |
| 100 | | 100 | 0.00 | |
| LE radius: 1.58 percent chord Slope of radius through LE: 0.20 | | | | |

| Slope of radius through LE: 0.20

2.1 Model Development

Two airfoil models, the conventional and the bumpy airfoils, were created. Each airfoil model, the C-grid fluid domain and the mesh were created in GAMBIT 2.3 modeling software.

2.1.1 Airfoil Modeling

The airfoil coordinates (Table 1) were imported into GAMBIT and first created a two-dimensional (2D) cross-section profile bounded by (upper and lower) edges. The edges were swept (or extruded) along the z-axis to a depth of 0.1m span and created another opposite face together with additional upper and lower faces. These faces formed a three-dimensional aerofoil that includes exactly six edges and four faces. For the bumpy airfoil, the LE is replaced by a sinusoidal edge before creating faces by using Nurbs line function in the software.



Figure 1 The Airfoil models created

2.1.2 Modeling of Flow Domain

The C-grid flow domain was created with a distance of 20 times chord length (20C) upstream of LE, 20C downstream of the trailing edge, and a height of 20C for the upper and lower domain. This was done using GAMBIT geometry controls. The C-grid was extruded along the z-axis to a depth equal to that of the airfoil span (0.1m)

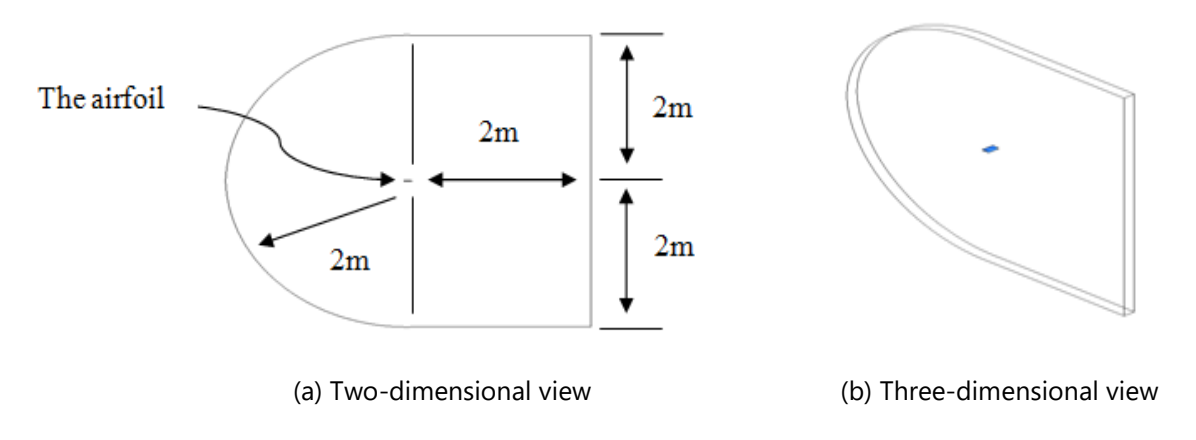


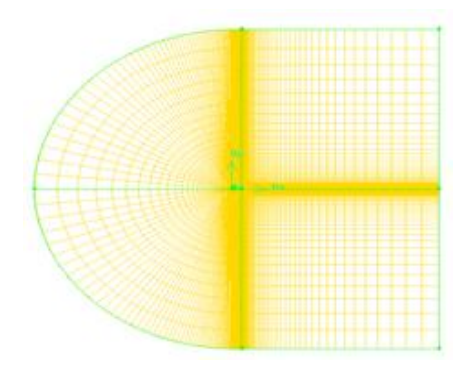
Figure 2. The fluid domain (C-grid)

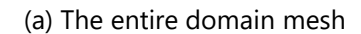
2.1.3 Mesh Generation

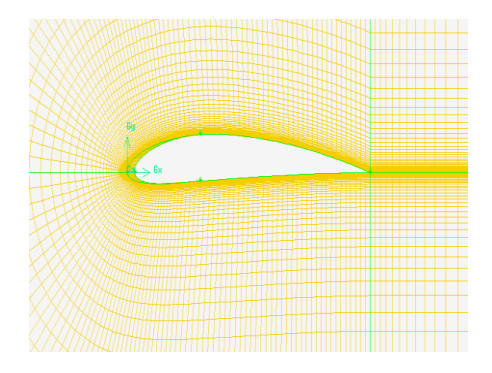
Four volumes were created within the computational domain and meshed. The airfoil's surface fluid boundary layer requirement was first determined. A Y+ value of 1 is used in determining the grid spacing at the boundary layer for all airfoils in this simulation; this help resolve the boundary layer accurately. Using a Y_+ value of 1 and a chord length of 0.1m, the normal wall distance (Y) is calculated approximately as 4.1e-5m or 0.000041m. Figure 3 show how the mesh is affected by the first cell grid spacing (Y= 4.1e-5m) and the subsequent cell geometric expansion of 1.2.

All the faces of the domain sub-volumes were meshed. Each region of the volumes was then meshed with a structured scheme; the entire cells are hexahedral with 875000 cells in total for all models.

The faces that made up the boundary of the computational domain were defined before exporting the mesh into FLUENT solver. These boundary types are the airfoil wall, the inlet, the outlet, and the symmetry boundaries.







(b) The mesh around the airfoil

Figure 3. The mesh

2.2 The Computational Approach

GAMBIT 2.3, as earlier mentioned, was used for the modeling and meshing. GAMBIT is an integrated preprocessor for CFD analysis which can be used to build geometry and generate mesh, or import a geometry created by a third-party CAD package, make modifications, and generate a mesh [11].

Fluent 6.3 was used for all the simulations, and it is a computational fluid dynamics (CFD) software package to simulate fluid flow problems. It uses the finite volume method to solve the governing fluid dynamics equations. It provides the capability to use different physical models such as incompressible or compressible, inviscid or viscous, laminar or turbulent, etc. [12]. SST $k-\omega$ turbulence model available in the fluent was used.

2.3 The Governing Fluid Flow Equations

The three fundamental equations of mass (continuity), momentum, and energy conservation that govern the fluid motion are given respectively by Nasser and Javad, [13]:

$$\frac{\partial \rho}{\partial t} + \nabla \cdot (\rho V) = 0 \tag{1}$$

$$\rho \frac{\partial V}{\partial t} + V.\nabla(\rho V) = \nabla \cdot \tau_{ij} - \nabla P + \rho F \tag{2}$$

$$\rho \frac{De}{Dt} + P(\nabla \cdot V) = \frac{\partial Q}{\partial t} - \nabla \cdot Q + \Phi$$
(3)

Depending on the physical nature of the fluid motion, one or more terms might be neglected. For example, if the flow is incompressible, and the coefficient of viscosity of the fluid, μ , as well as coefficient of thermal conductivity is constant, the continuity, momentum, and energy equations reduce to the following equations respectively [13]:

$$\nabla . V = 0 \tag{4}$$

$$\rho \frac{\partial V}{\partial t} + \rho V \nabla \cdot V = \mu \nabla^2 V - \nabla P + \rho F \tag{5}$$

$$\rho \frac{De}{Dt} = \frac{\partial Q}{\partial t} + k \nabla^2 T + \Phi \tag{6}$$

The appropriate solution algorithm and the numerical procedure are determined by the presence of each term and their combination.

Other important fluid dynamic equations are the Reynolds average Navier-Stokes (RANS) equations. The idea behind the equation is Reynolds decomposition, whereby an instantaneous quantity is decomposed in to its time-average and fluctuating quantities, an idea first proposed by Osborne Reynolds. Also, Reynolds average Navier-Stokes (RANS) equations The RANS equations are primarily used to describe turbulent flows.

These equations can be used with approximations based on knowledge of the properties of flow turbulence to give approximate time averaged solutions to the Navier-Stokes (N-S) equations. Each instantaneous quantity in the N-S equation can be split into time-averaged and fluctuating components, and the resulting equation time averaged, to yield (for incompressible flow) [12]:

$$\nabla.\,\bar{V} = 0 \tag{7}$$

$$\frac{\partial \overline{v}}{\partial t} + \overline{V} \nabla \cdot \overline{V} = \frac{\mu}{\rho} \nabla^2 \overline{V} - \frac{1}{\rho} \nabla \cdot \overline{P} + \overline{F} - \overline{\nabla \cdot V^{12}}$$
 (8)

Additional modeling is required by the non-linear Reynolds stress term $(\overline{\nabla}.V^{t^2})$ to close the RANS equation for solving and has led to the creation of many different turbulence models.

Standard k- ω model is two-equation turbulence model solving for k and ω , the specific dissipation rate (ϵ/k) based on Wilcox (1998). The model demonstrates superior performance for wall-bounded and low Reynolds number flows. It shows potential for predicting transition. The equations are [12]:

$$\mu_t = \alpha^* \rho \frac{k}{\omega} \tag{9}$$

$$\rho \frac{Dk}{Dt} = \tau_{ij} \frac{\partial \overline{u}}{\partial y} - \rho \beta^* f_{\beta^*} k \omega + \frac{\partial}{\partial y} \left[\left(\mu + \frac{\mu_t}{\sigma_k} \right) \frac{\partial k}{\partial y} \right]$$
 (10)

$$\rho \frac{D\omega}{Dt} = \alpha \frac{\omega}{k} \tau_{ij} \frac{\partial \bar{u}}{\partial y} - \rho \beta^* f_{\beta} \omega^2 + \frac{\partial}{\partial y} \left[\left(\mu + \frac{\mu_t}{\sigma_{to}} \right) \frac{\partial \omega}{\partial y} \right]$$
(11)

$$\omega \approx \frac{\varepsilon}{k} \propto \frac{1}{\tau}$$

SST $k-\omega$ model is a variant of the standard $k-\omega$ model. It's the model used in this study. The model combines the original Wilcox model for use near walls and the standard $k-\varepsilon$ model away from wall using a blending function. Also limits turbulence viscosity to guarantee that $\tau_t \sim k$. The transition and shearing options are borrowed from standard $k-\omega$. The resulting blended equations are [12]:

$$\rho \frac{Dk}{Dt} = \tau_{ij} \frac{\partial \overline{u}}{\partial y} - \rho \beta^* k \omega + \frac{\partial}{\partial y} \left[\left(\mu + \frac{\mu_t}{\sigma_k} \right) \frac{\partial k}{\partial y} \right]$$
 (12)

$$\rho \frac{D\omega}{Dt} = \frac{\gamma}{\nu_t} \tau_{ij} \frac{\partial \overline{u}}{\partial y} - \rho \beta^* \omega^2 + \frac{\partial}{\partial y} \left[\left(\mu + \frac{\mu_t}{\sigma_{\omega}} \right) \frac{\partial \omega}{\partial y} \right] + 2\rho (1 - F_1) \sigma_{\omega 2} \frac{1}{\omega} \frac{\partial k}{\partial y} \frac{\partial \omega}{\partial y}$$
(13)

$$\phi = F_1 \phi_1 + (1 - F_1) \phi_1 \quad ; \qquad \qquad \phi = \beta, \ \sigma_k, \ \sigma_{\omega}, \ \gamma$$

The Lift and drag coefficients of an airfoil are given respectively as [1]:

$$C_L = \frac{L}{\frac{1}{2} \rho U_0^2 C} \tag{14}$$

$$C_D = \frac{D}{\frac{1}{2} \rho U_0^2 C} \tag{15}$$

2.4 Simulation Set-up and boundary conditions

The pressure-based (segregated and coupled) solver was used to perform the simulations in fluent with higher order spacial discretization. The semi-implicit method for pressure linked equations (SIMPLE) algorithm was used for pressure velocity coupling. Second-order upwind scheme was implemented for discretizing the equations and PRESTO was used as the pressure interpolation scheme. Default underrelaxation factors provided in the solver were used. Boundary types used in this study are: velocity inlet, symmetry, wall, and pressure outlet. The flow type is incompressible with a Reynolds number of 41075.22 (this

corresponds with 6 m/s inlet velocity and 0.1 m airfoil chord length), a temperature of 300K and a constant air density of 1.225kg/m³ at a pressure of 1 atmosphere. Shear Stress Transport K-Omega turbulence model was used in the simulation. The turbulent intensity of 1% and turbulent viscosity of 10 were used.

The simulation is assumed to be a steady state pressure-based one and was carried out using segregated solver. Reference values were specified to monitor lift and drag forces and a convergence criterion of $1*10^{-6}$ is set for the residuals. The AoA range is 0, 5, 10, 15, 20 and 25 degree.

In order to obtain the pressure and velocity fields within the fluid domain, and hence to calculate for lift and drag forces and coefficients by solving the governing fluid dynamic equations by the software, boundary conditions were specified. The inlet air velocity was specified as the free air stream velocity (U_o), the fluid velocity differential through the symmetry boundaries (i.e. the other two sides of the computational domain) are zero (∇ . V = 0), and the fluid velocity at the airfoil wall was specified as zero.

3. Results and Discussion

The numerical results obtained from the simulation of the airfoil models are presented in graphs. The results of the simulation are also viewed by generating pressure and velocity contour plots of domain using fluent post processing tool.

3.1 Lift and Drag coefficients

Figure 4 shows the comparison of lift coefficients for the bumpy and conventional airfoils models as AoA is varied from 0 to 25 degree, while the comparison of variation of drag coefficients with AoA for the two models are represented in the Figure 5.

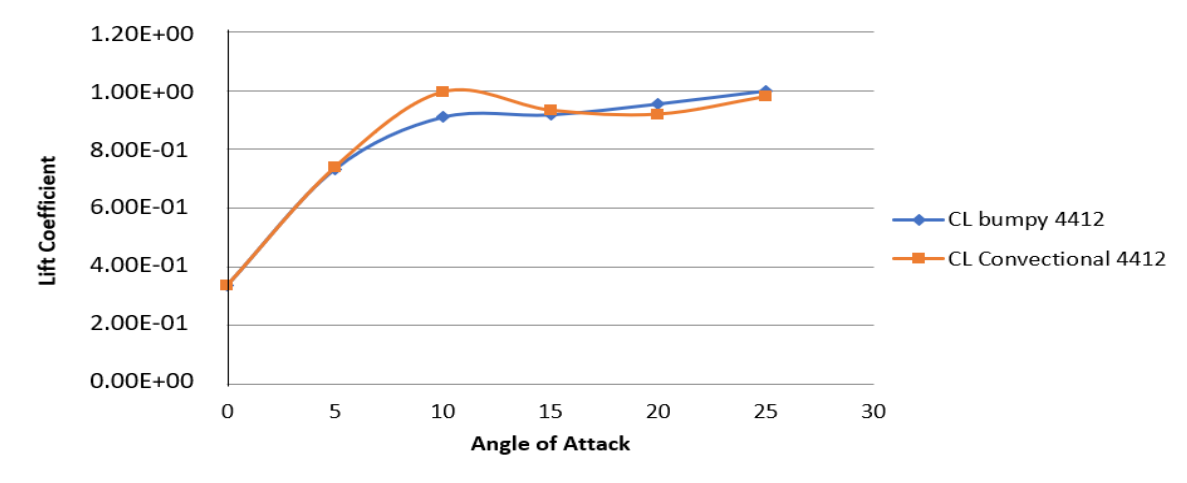


Figure 4. Lift coefficients versus AoA

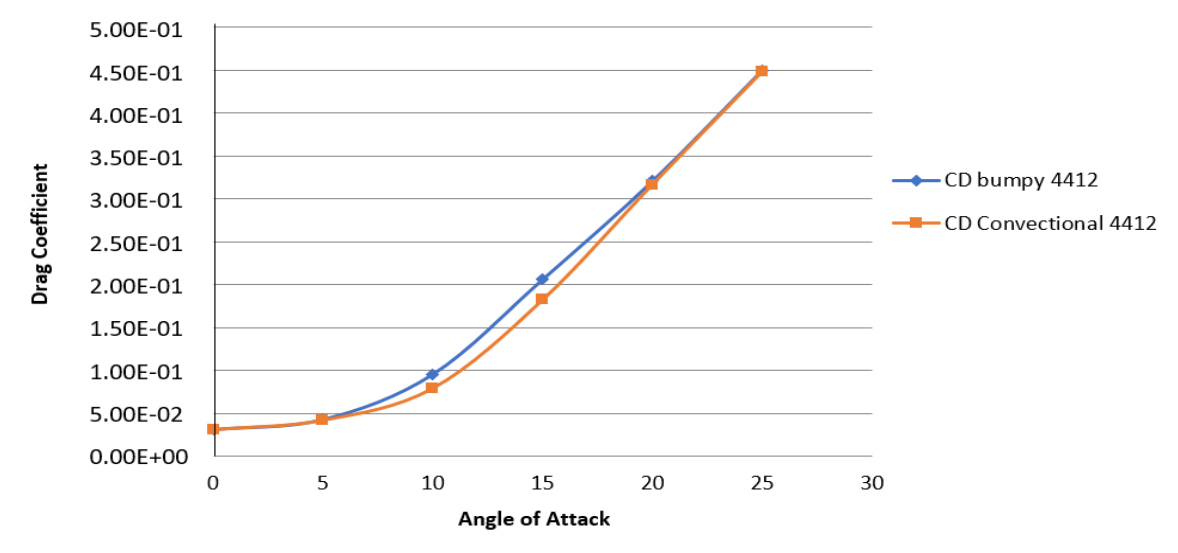


Figure 5. Drag coefficients versus AoA

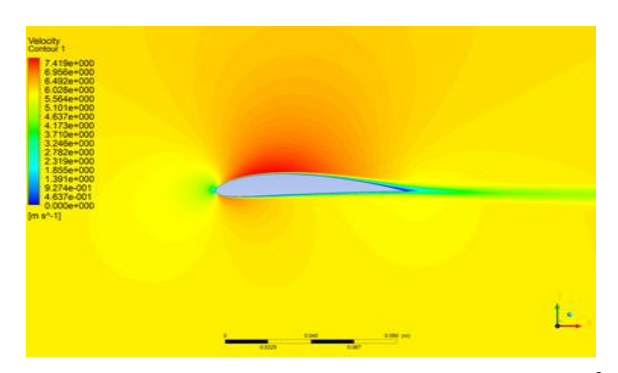
In Figure 4, it was found that for the convectional airfoil, stall (drop of lift coefficient) started at around 12-degree AoA, but for the bumpy airfoil, on reaching the maximum lift coefficient at the same angle, the value remain approximately the same with increasing AoA up to 15-degree; its lift curve did not drop but stayed leveled after 12-degree. The lift curve for the convectional model achieved a higher maximum lift coefficient than the bumpy airfoil but quickly dropped until the lift coefficients of the two models are the same at around 17-degree AoA. The minimum lift coefficient for the convectional and the bumpy airfoils is approximately 0.35 at 0-degree AoA. The max lift coefficient for the convectional airfoil is 1, and that of bumpy one stayed at a maximum of 0.91 before increasing after 15-degree AoA. After15-degree, the convectional airfoil curve dipped below the bumpy airfoil curve, that is, the lift coefficient of the bumpy airfoil is greater than that of the conventional at angles of attack greater than 15-degree.

The drag curve (Figure 5) of the conventional airfoil shows that drag coefficient increases with AoA up to 15-degree, and continue to increase along a straight line up to the last angle (25-degree). The drag curve of the bumpy airfoil model shows similar trend with that of conventional one, only that between 5 and 20-degree AoA, the bumpy airfoil has greater drag coefficients. The lowest and highest drag coefficients for both models are approximately 0.03 (at 0-degree AoA) and 0.44 (at 25-degree AoA) respectively.

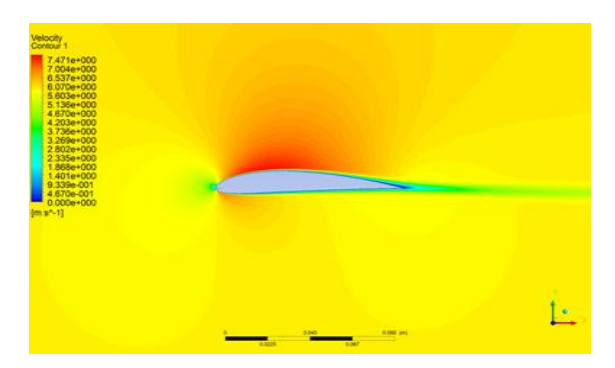
3.2 Velocity Contours

Typically, high-pressure region exists beneath the airfoil model, while the top of the airfoil is the low-pressure region. As a result, at the trailing edge, air flow from the bottom surface of the airfoil to the top surface, and creates a low-pressure region which is much lower than the pressure on the top surface. This creates favorable pressure gradient in the front part but an adverse pressure gradient in the rear part, and hence slows down the velocities inside the boundary layer which causes the recirculation region close to the top surface of airfoil. The recirculation region grow upstream as more air is accelerated from bottom to top surface of airfoil (Kunya et al. 2021).

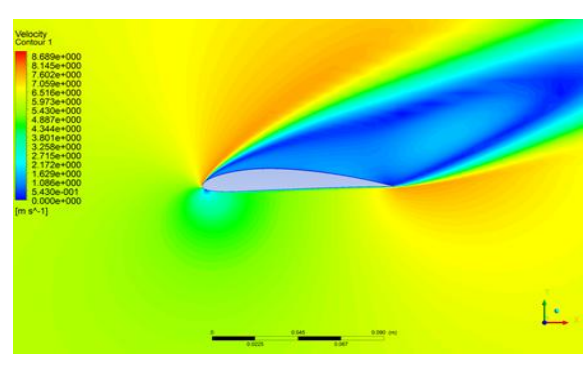
The contours of velocity at 0° and 20° AoA for the conventional and bumpy airfoils are compared as shown in Figure 6. Flow over the airfoil boundaries is intact at the angle of 0°; there is no flow separation, and this is the reason why the lift curves are aligned for both conventional and bumpy airfoils at that angle up to 5° AoA. Beyond 5°-AoA flow separation starts for all the airfoils and increases with AoA, the effects of drag become dominant and the airfoil enters stall conditions. At 20° AoA, flow separation is delayed for the airfoil with LE bumps. Study revealed that bumps along the LE produced stream-wise vortices which carry higher momentum flow in the boundary layer and keep the flow attached to the surface of the airfoil and, in turn delayed separation, and thus increasing the airfoil operating angle (Kunya et al. 2021).

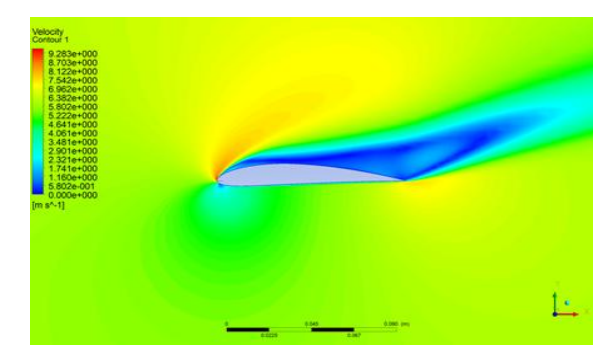


(a) Velocity contours for convectional airfoil at 0°



(b) Velocity contours for bumpy airfoil at 0°





(c) Velocity contours for convectional airfoil at 20°

(d) Velocity contours for bumpy airfoil at 20°

Figure 6. Velocity contour

4. Conclusion

This study investigated the effect of sinusoidal bumps at the leading edge of an airfoil with a NACA 4412 cross-section profiles at low Reynolds number (41075.22) using numerical method. The result of the study shows that the airfoil without LE bumps, the convectional airfoil model, achieved a higher maximum lift coefficient than the bumpy airfoil between 5-degree and 15-degree angles of attack but quickly dropped below that of the bumpy airfoils due to stall effects. The max lift coefficient for the convectional airfoil is 1 at around 12-degree AoA, and that of bumpy one stayed at a max of 0.91 from 12-degree to 15-degree AoA. The bumpy airfoil showed increased maximum lift coefficient and a larger AoA beyond 15-degree than the conventional airfoil. This could be due to production of stream-wise vortices along the airfoil leading edge by the LE bumps. The drag coefficient of the conventional airfoil increases with angle of attack up to 15-degree, and continue to increase along a straight line up to the last angle (25-degree). The bumpy airfoil model drag coefficients variation with angle of attack shows similar trend with that of conventional one, only that between 5 and 20-degree angle of attack, the bumpy airfoil has greater drag coefficients. The lowest and highest drag coefficients for both models are approximately 0.03 and 0.44.

The analysis revealed that an aerodynamic system like wind turbine blade(s) with conventional (straight) leading edge operating in low wind speed area, can perform better at normal operating angle of attack. However, during stall regulation of a wind turbine, the condition at which the blade angle of attack is increased to a higher angle, blade with bumpy (sinusoidal) airfoil would perform better. It is therefore recommended to design a mechanism that automatically introduce bumps at the blade leading edge in an appropriate aerodynamic condition.

References

- [1] J. Douglas, J. Gasiorek, J. Swaffield, and L. Jack, "Fluid Mechanics," Published by Pearson Prentice Hall," 2005.
- [2] C. Thumthae and T. Chitsomboon, "Optimal Angle of Attack for Untwisted Blade Wind Turbine," Renewable Energy, 34, pp. 1279-1284, 2009.
- [3] F.E. Fish and J.M. Battle, "Hydrodynamic Design of the Humpback Whale Flipper," Journal of Morphology, Volume 225. Pp 51-60, 1995.
- [4] K.L. Hansen, R.M. Kelso and B.B. Dally, "Performance Variations of Leading-Edge Tubercles for Distinct Airfoil Profiles," AIAA Journal, Volume 49, No. 1, pp 185-194, 2011.
- [5] A.F.A. Gawad, "Numerical Simulation of the Effect of Leading-Edge Tubercles on the Flow Characteristics Around an Airfoil," *International Mechanical Engineering Congress & Exposition*, 2012.

- [6] M. Asli, B.M. Gholamali, and A.M. Tousi, "Numerical Analysis of Wind Turbine Airfoil Aerodynamic Performance with Leading Edge Bump," Mathematical Problems in Engineering, 2015. http://dx.doi.org/10.1155/2015/493253.
- [7] B.I. Kunya, C.O. Folayan, G.Y. Pam, F.O. Anafi, and N.M. Muhammad, "Experimental and Numerical Study of the Effect of Varying Sinusoidal Bumps Height at the Leading Edge of the NASA LS (1)-0413 Airfoil at Low Reynolds Number," CFD Letters 11, no.3 (2019): 129-144, 2019.
- [8] B.I. Kunya, A.B. Aliyu and B.M. Salihu, "Aerodynamic Performance of the NACA 63-012 Airfoil with Sinusoidal-Shaped Leading Edge at Low Air Velocity," Nigerian Research Journal of Engineering and Environmental Sciences 5(2), pp. 644-658, 2020.
- [9] B.I. Kunya, C.O. Folayan, G.Y. Pam, and F.O. Anafi, "A Numerical Study on the Effect of Bumps Spacing at the Leading Edge of Whale inspired NASA LS (1)-0413 Aerofoil at Low Wind Speed," Bayero Journal of Engineering and Technology (BJET)16, no.1, pp 119-132, 2021.
- [10] K. Laurence, Jr. Loftin, and A.S. Hamilton, "Aerodynamic Characteristics of 15 NASA Aerofoil Sections at Seven Reynolds Number From 0.7x10⁶ to 9.0 x10⁶" Langley Aeronautical Laboratory, Langley Air Force Base, Va. National Advisory Committee for Aeronautics (NASA) Technical Notes, Washington, 1949.
- [11] GAMBIT 2.3, "Introductory Notes," Fluent User Services Centre, 2006. www.fluentusers.com.
- [12] Fluent 6.3, "Introductory Notes". Fluent User Services Centre, 2006. www.fluentusers.com
- [13] A. Nasser and M. Javad, "An Introduction to Computational Fluid Dynamics" Chapter 20 in Fluid Flow Handbook. Department of Mechanical and Industrial Engineering. University of Toronto, 2012. www.ewp.edu/hartford/~ernesto/F2012